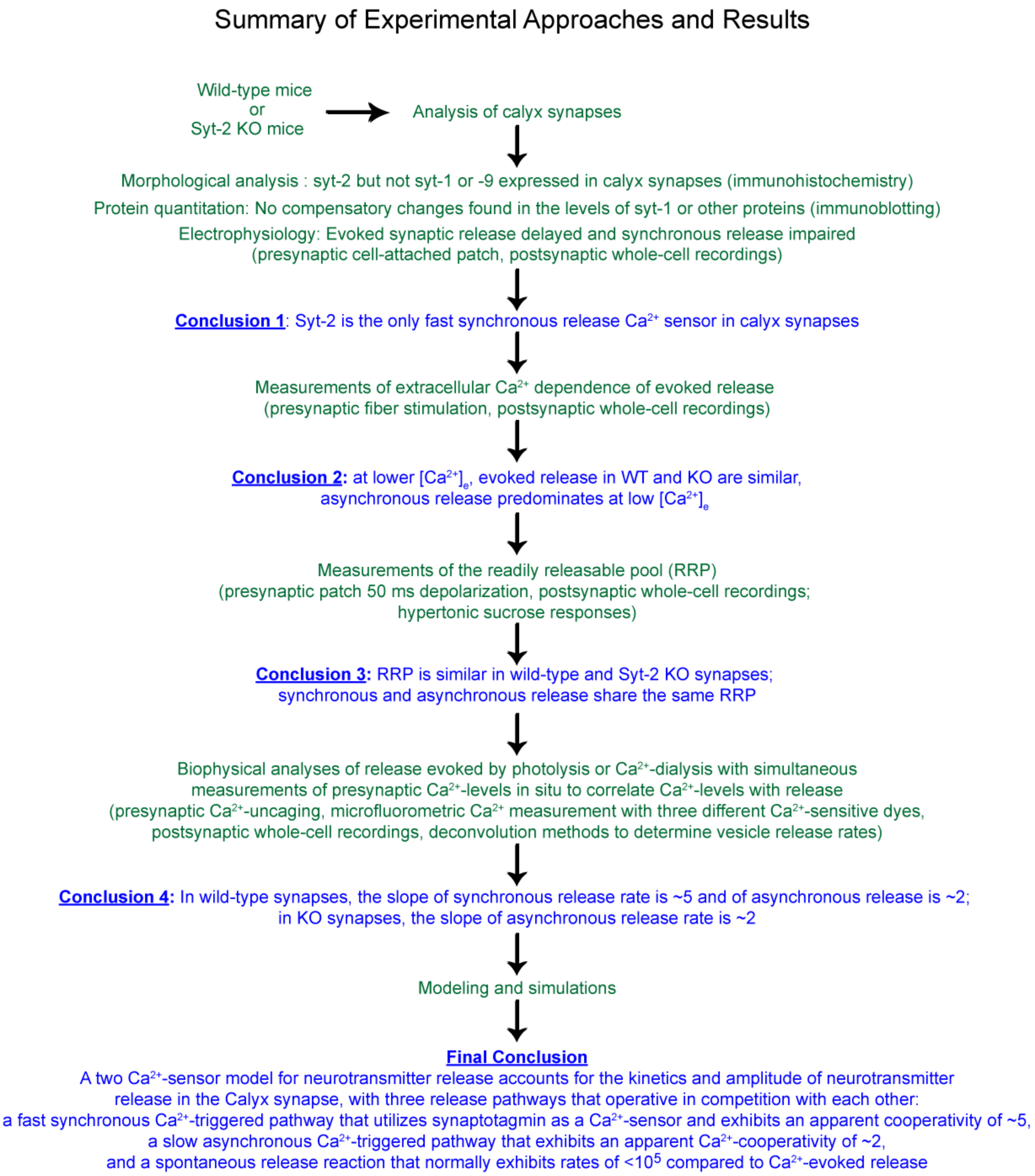

Summary of Experimental Approaches and Results

Wild-type mice
or
Syt-2 KO mice

Analysis of calyx synapses

Morphological analysis : syt-2 but not syt-1 or -9 expressed in calyx synapses (immunohistochemistry)

Protein quantitation: No compensatory changes found in the levels of syt-1 or other proteins (immunoblotting)

Electrophysiology: Evoked synaptic release delayed and synchronous release impaired
(presynaptic cell-attached patch, postsynaptic whole-cell recordings)

Conclusion 1: Syt-2 is the only fast synchronous release Ca^{2+} sensor in calyx synapses

Measurements of extracellular Ca^{2+} dependence of evoked release
(presynaptic fiber stimulation, postsynaptic whole-cell recordings)

Conclusion 2: at lower $[Ca^{2+}]_e$, evoked release in WT and KO are similar,
asynchronous release predominates at low $[Ca^{2+}]_e$

Measurements of the readily releasable pool (RRP)
(presynaptic patch 50 ms depolarization, postsynaptic whole-cell recordings;
hypertonic sucrose responses)

Conclusion 3: RRP is similar in wild-type and Syt-2 KO synapses;
synchronous and asynchronous release share the same RRP

Biophysical analyses of release evoked by photolysis or Ca^{2+}-dialysis with simultaneous
measurements of presynaptic Ca^{2+}-levels in situ to correlate Ca^{2+}-levels with release
(presynaptic Ca^{2+}-uncaging, microfluorometric Ca^{2+} measurement with three different Ca^{2+}-sensitive dyes,
postsynaptic whole-cell recordings, deconvolution methods to determine vesicle release rates)

Conclusion 4: In wild-type synapses, the slope of synchronous release rate is ~5 and of asynchronous release is ~2;
in KO synapses, the slope of asynchronous release rate is ~2

Modeling and simulations

Final Conclusion

A two Ca^{2+}-sensor model for neurotransmitter release accounts for the kinetics and amplitude of neurotransmitter
release in the Calyx synapse, with three release pathways that operative in competition with each other:
a fast synchronous Ca^{2+}-triggered pathway that utilizes synaptotagmin as a Ca^{2+}-sensor and exhibits an apparent cooperativity of ~5,
a slow asynchronous Ca^{2+}-triggered pathway that exhibits an apparent Ca^{2+}-cooperativity of ~2,
and a spontaneous release reaction that normally exhibits rates of $<10^5$ compared to Ca^{2+}-evoked release

Supplementary Figure 1

Summary of Experimental Approaches and Results. Schematic overview of the entire content and conclusions of the present paper, starting with the use of wild-type and synaptotagmin-2 KO (Syt-2 KO) mice, and ending with the quantitative description of the entire release process.

Supplementary Figure 2a

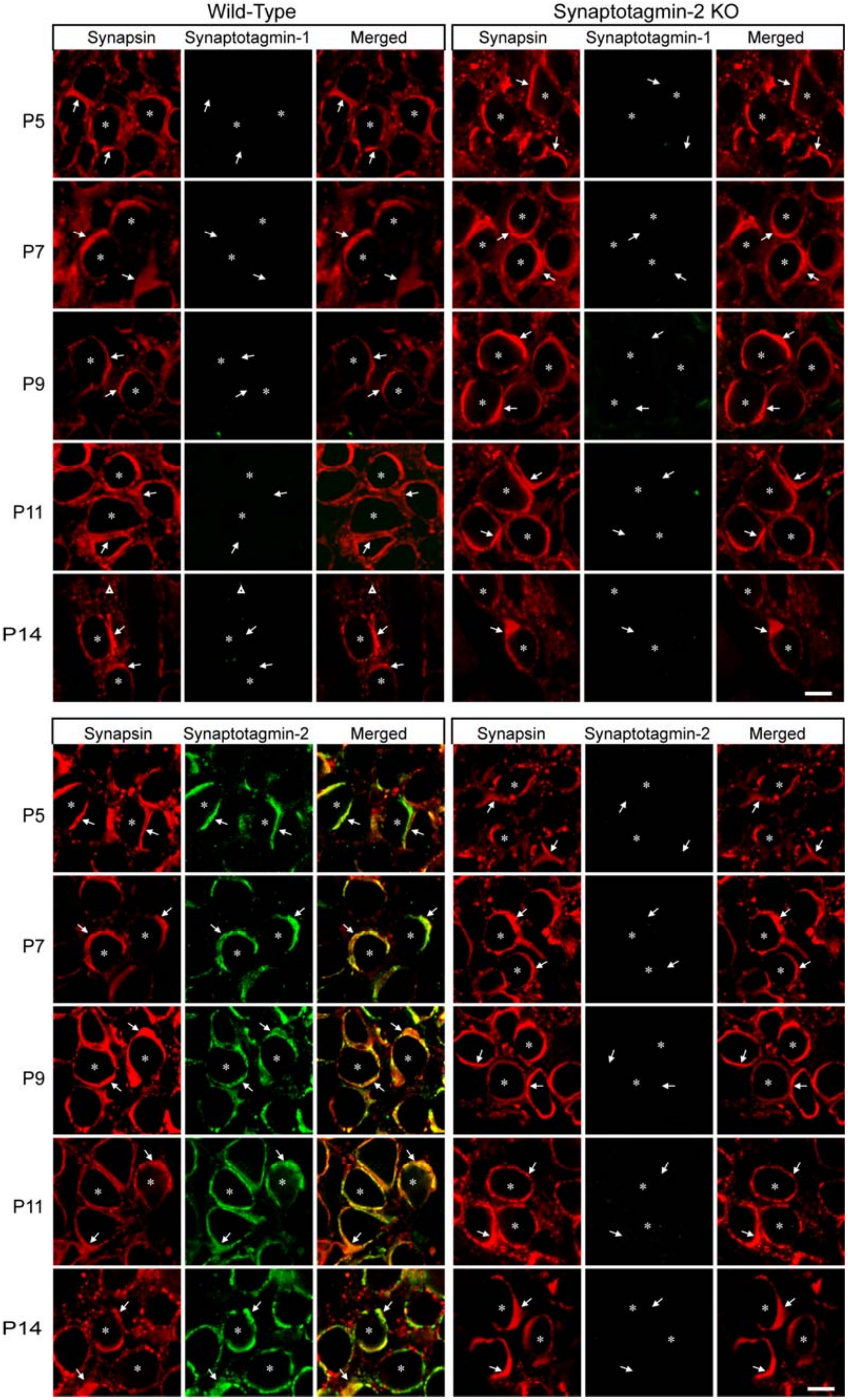

Supplementary Figure2b

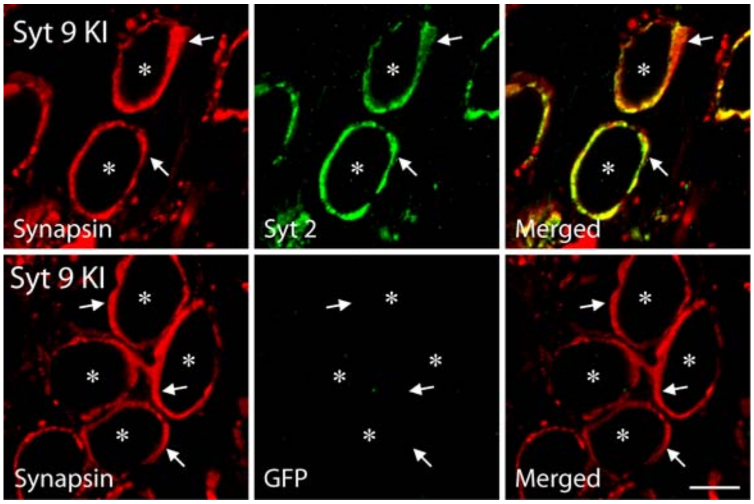

Supplementary Figure 2

Analysis of synaptotagmin-1, -2, and -9 expression in presynaptic calyx terminals

Double immunofluorescence labeling of brainstem sections, using antibodies to synapsins (red; left panels) and to synaptotagmins (green; center panels). The right panels display merged images (yellow = staining overlap). Asterisks identify postsynaptic cell bodies; arrows indicate presynaptic terminals; open triangles indicate synaptotagmin-1 positive terminals.

a. Comparison of synaptotagmin-1 and -2 expression in wild-type and synaptotagmin-2 KO mice at postnatal days P5 to P14.

b. Analysis of synaptotagmin-9 expression in the calyx of knock-in (KI) mice which express GFP-tagged synaptotagmin-9 (ref. 15). Note that direct immunofluorescence localization of synaptotagmin-9 is not possible because of a lack of specific antibodies, but we found that the GFP-fusion protein of synaptotagmin-9 is functional, allowing the use of the KI mice with staining for GFP to immunolocalize synaptotagmin-9.

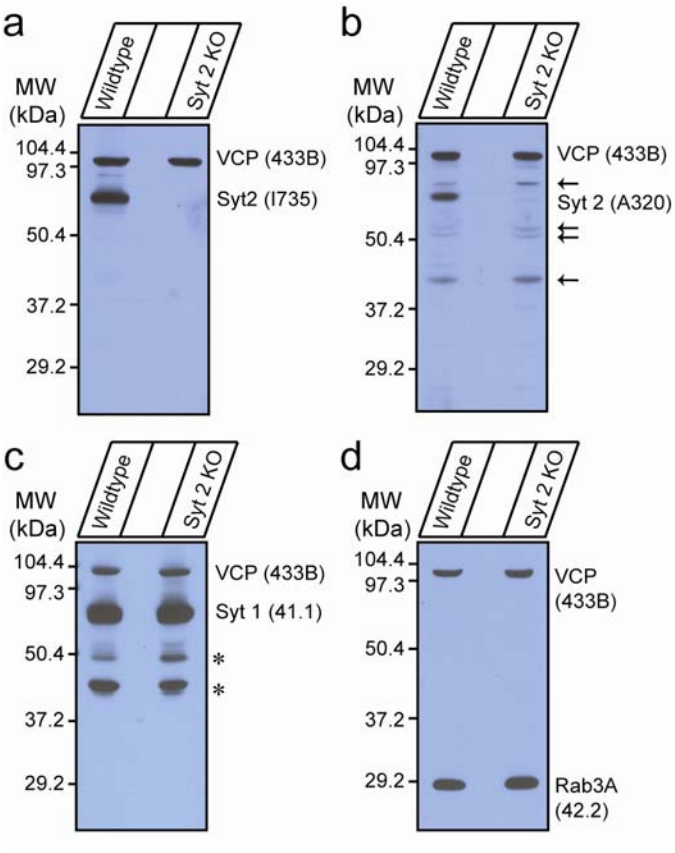

Supplementary Figure 3

Immunoblot analysis of synaptotagmin-2 in brainstem samples from the MNTB of synaptotagmin-2 KO mice

a. Immunoblots of brainstem homogenates from synaptotagmin-2 KO and littermate control mice using polyclonal antibody I735 (dilution = 1:4,000) that was raised against the double C_2-domain fragment of synaptotagmin-2. The immunoblot indicates there is a total lose of synaptotagmin-2 signal, whereas VCP levels examined on the same membrane were unchanged.

b. Immunoblots of brainstem homogenates using polyclonal antibody A320 (dilution = 1:500) that was raised against the intravesicular N-terminal region of synaptotagmin-2. VCP was again used as a loading control. Note that the A320 antiserum non-specifically reacts with unidentified proteins as indicated by arrows.

c. and **d.** Immunoblots of brainstem homogenates using antibodies to synaptotagmin-1 (c) or Rab3A (d) as control synaptic vesicle proteins.

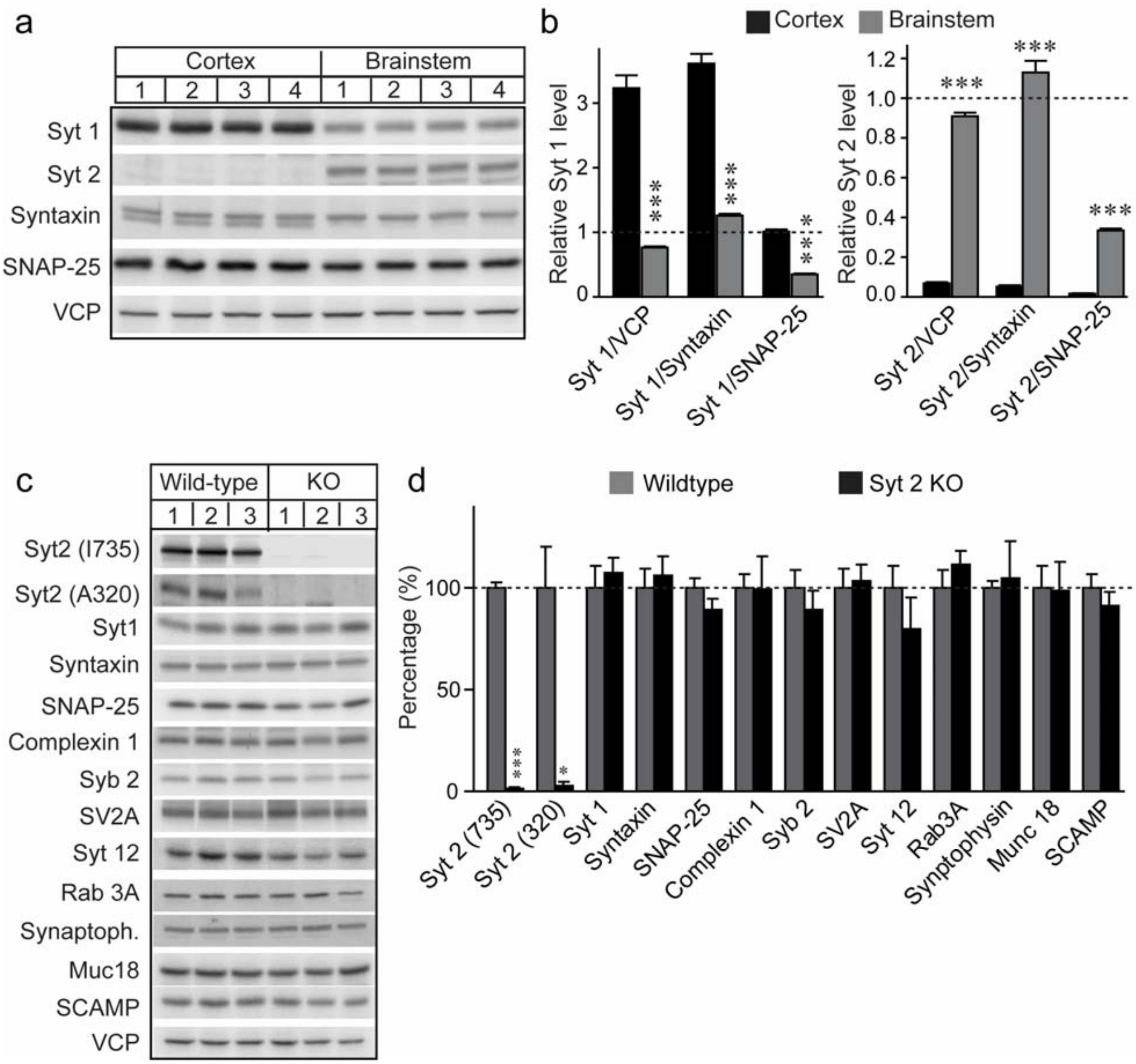

Supplementary Figure 4

Protein quantitation in wild-type mouse and synaptotagmin-2 KO mice.

a. and **b**. Immunoblot analysis of synaptotagmin-1 and -2 in homogenates obtained from cortex and from the MNTB-region of the brainstem of wild-type mice. Panels show representative immunoblots (a) and summary graphs of protein levels (b). For the brainstem homogenates, a 200 μm region in the MNTB was microdissected. The levels of synaptotagmin-1 and -2, syntaxin-1, SNAP-25, and VCP were quantified using ^{125}I-conjugated secondary antibodies and phosphoImager detection. Synaptotagmin-1 and -2 levels were then normalized to those of VCP, syntaxin and SNAP25, respectively, measured on the same immunoblot membrane to determine the relative amount of synaptotagmin-1 and -2 expression in the cortex and MNTB-region of wild-type mice.

c. and **d.** Immunoblot analysis of synaptic proteins in the microdissected MNTB region from the brainstem of wild-type and synaptotagmin-2 KO mice. Panels show representative blots (c) and summary graphs of protein levels (d). Protein levels were quantified using ^{125}I conjugated secondary antibodies with phosphoImager detection; all levels are normalized for those of VCP or GDI as internal controls. Data are presented as mean±SEM. *p <0.05; ***p<0.001

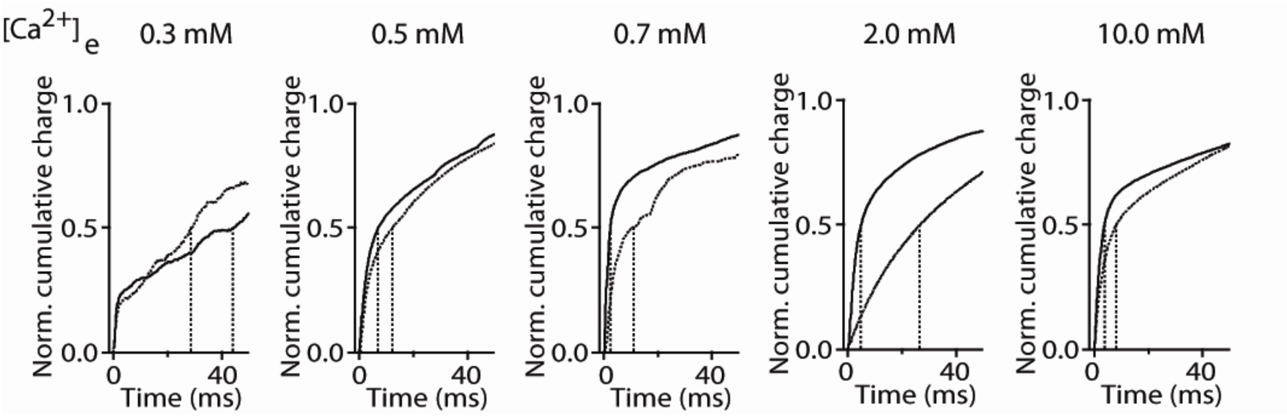

Supplementary Figure 5

Kinetics of neurotransmitter release evoked by isolated action potentials.

The graphs depict the average normalized EPSC charge transfer (integrated over 100 ms) from wild-type (solid curve) and synaptotagmin-2 deficient synapses (dashed curve) at the indicated [Ca^{2+}]$_e$**.** in the presence of AP-5 (50 μM).

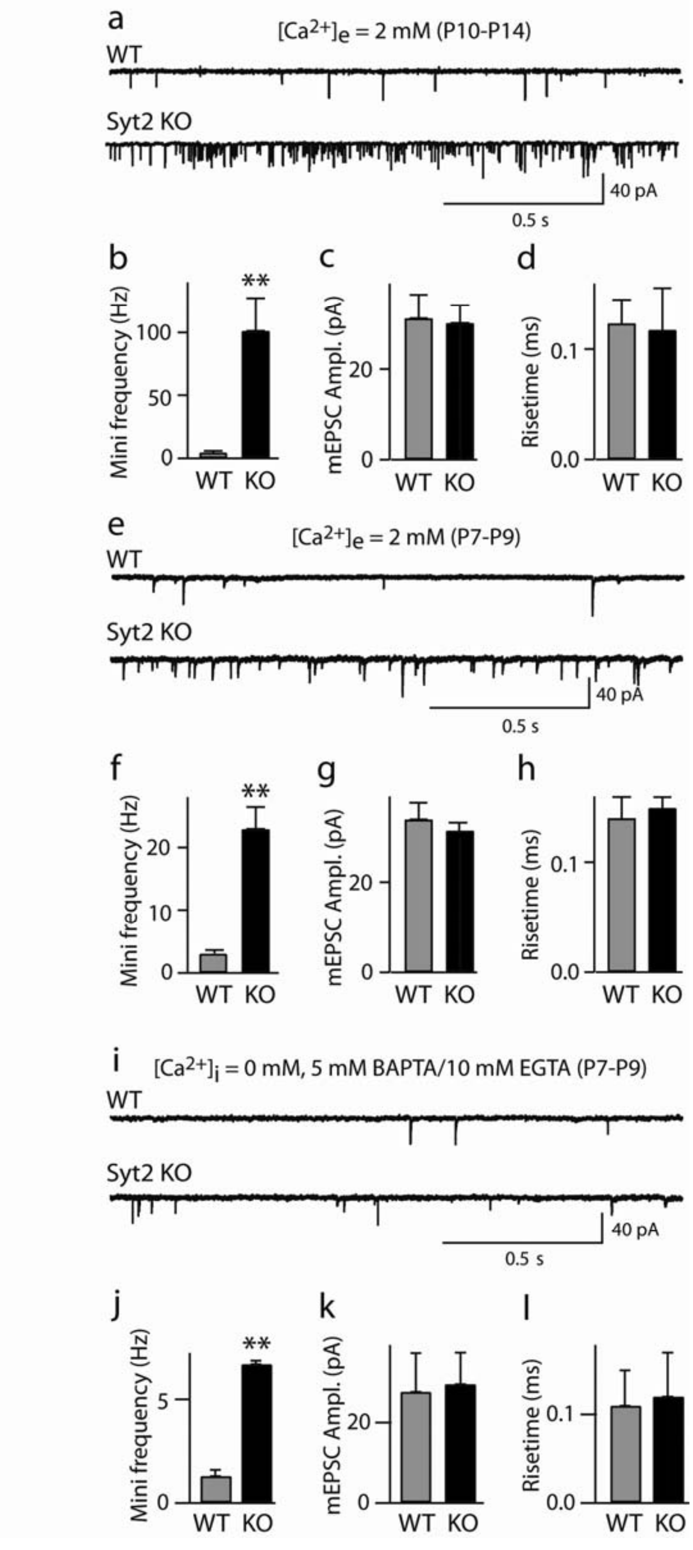

Supplementary Figure 6

Spontaneous neurotransmitter release in wild-type (WT) and synaptotagmin-2 KO neurons

a. Representative traces of mEPSCs recorded in MNTB neurons from wild-type (upper panel) and synaptotagmin-2 KO mice (lower panel) at P14.

b-d. Summary graphs of the frequency, amplitude and 20-80% risetimes of mEPSC at P10-P14 (n=11 WT and 12 KO terminals).

e. Representative traces of mEPSCs recorded in MNTB neurons from wild-type (upper panel) and synaptotagmin-2 KO mice (lower panel) at P8.
f-h. Summary graphs of the frequency, amplitude and 20-80% risetimes of mEPSC at P7-P9 (n=5 WT, and 7 KO terminals).
i. Representative traces of mEPSCs recorded in MNTB neurons in wild-type (upper panel) and synaptotagmin-2 mutant mice (lower panel) at postnatal day 7 in calyx terminals that were dialyzed with Ca^{2+}-free pipette solution (0 mM Ca^{2+}, 10 mM EGTA and 5 mM BAPTA).
j-l. Summary graphs of the frequency, amplitude and 20%-80% risetimes of mEPSC in Ca^{2+}-free terminals at P7-P9 (n=9 WT, and 11 KO terminals).

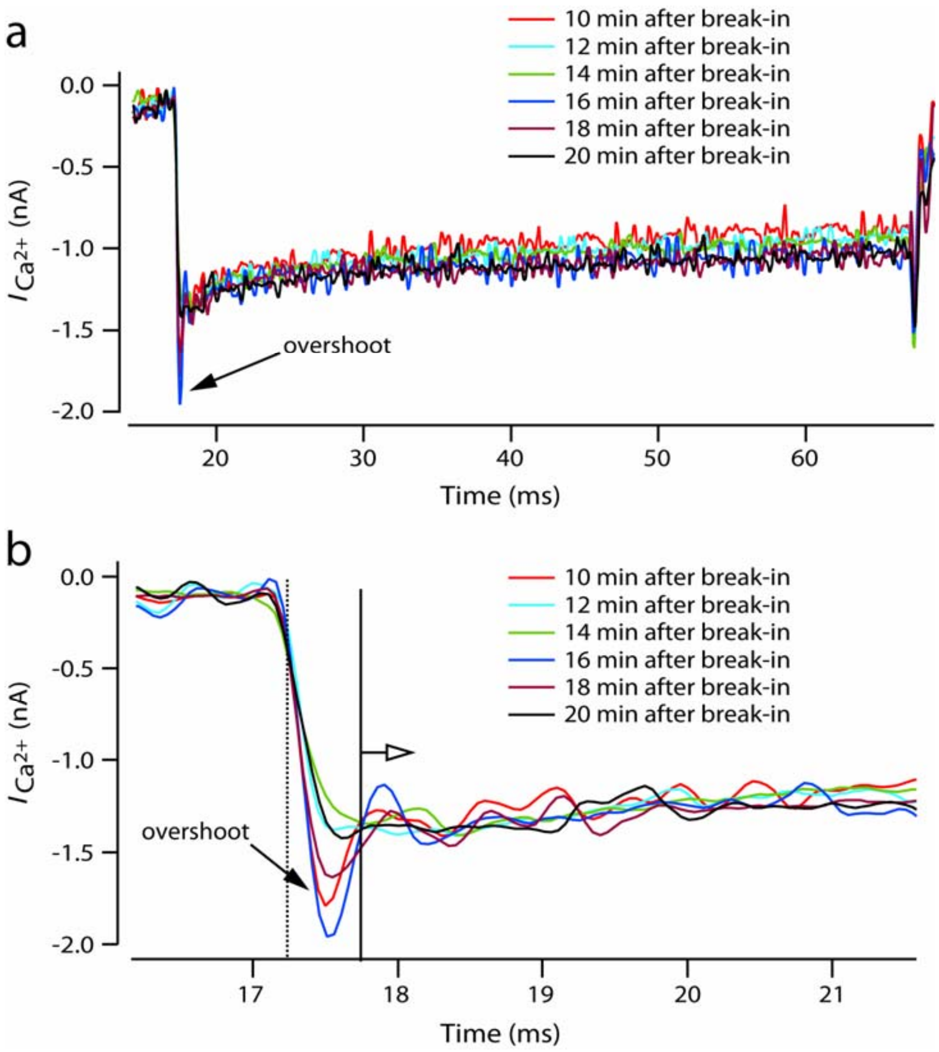

Supplementary Figure 7

Determination of the presynaptic Ca^{2+}-current amplitude in calyx terminals using the pre-depolatization protocol of Sakaba and Neher (2001)[4].

a. Representative traces recorded at different times after addition of tetrodotoxin to show that the initial Ca^{2+}-current overshoot obtained after shifting the voltage from the 4 ms pre-depolarization at +80 mV to +20 mV is variable. The overshoot (closed arrow) does not appear to be caused by residual Na^{+}-current activity because it still occurs after 10 min of 1 µM TTX application, and is not dependent on the time of TTX perfusion.

b. Enlargement of the initial phase in the traces of a. the shadowed area marks the time period used to determine the Ca^{2+}-current amplitude in Fig. 3b. To estimate the Ca^{2+}-current amplitude, we determined the maximum calcium current 0.6 ms after the onset of I_{Ca} (indicated by the open arrow).

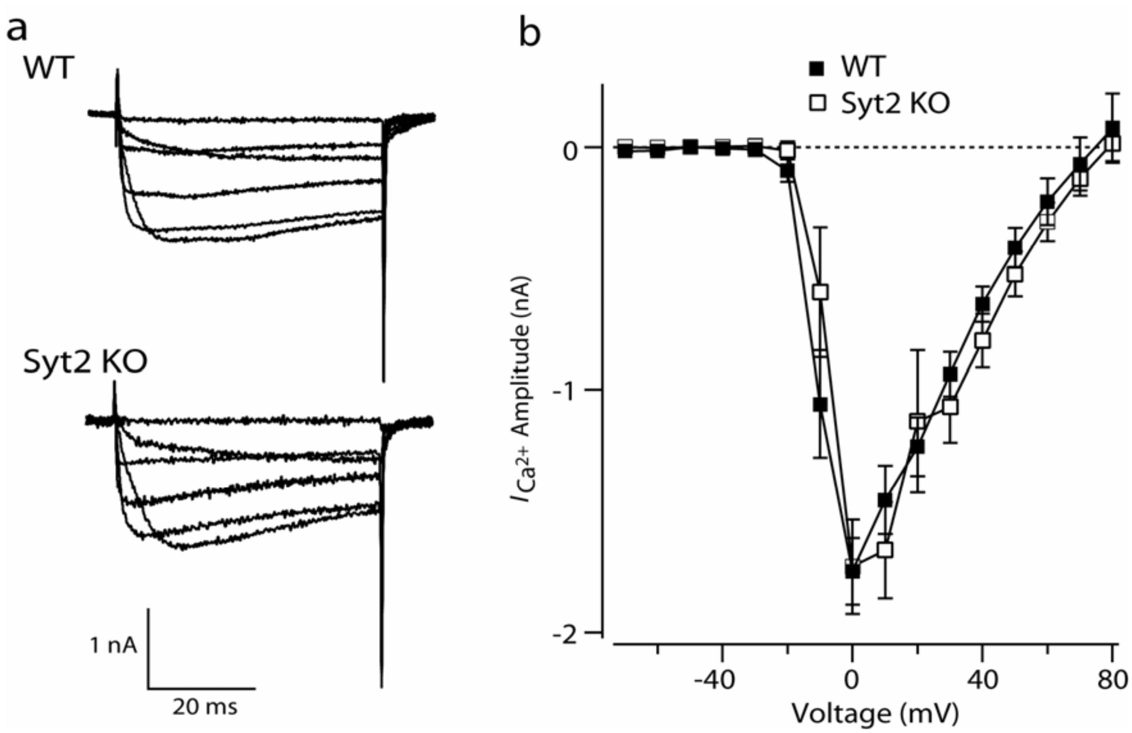

Supplementary Figure 8

Presynaptic Ca^{2+}-current recordings in calyx terminals without the pre-depolarization protocol.

Ca^{2+}-currents were recorded in calyx synapses in the presynaptic patch configuration at P7~P9 in the presence of 0.1 µM tetrodotoxin.

a. Representative traces of recordings of voltage-gated Ca^{2+}-currents in calyx terminals from wild-type (top) and synaptotagmin-2 KO mice (bottom) at P7-P9. The currents were recorded in response to depolarization from -80 mV to -30, -10, 0, 10, 30 and 50 mV.

b. Ca^{2+}-current/voltage relationship obtained from the 16 wild-type (open symbols) and 13 synaptotagmin-2 KO (filled symbols) calyx terminals.

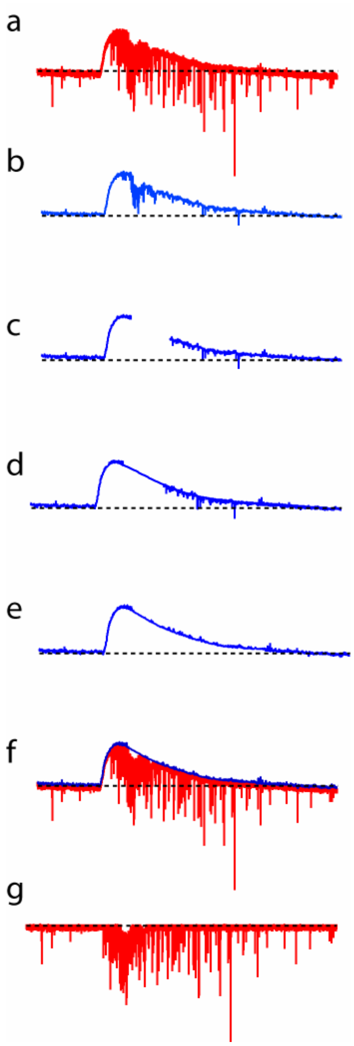

Supplementary Figure 9

Procedure for estimating the RRP using sucrose-triggered mEPSCs.

Puffing of 2 M of sucrose onto a calyx synapse always triggers a burst of mEPSCs but often induces a baseline drift in the same time. This drift is not a synaptic signal because it can also be induced by puffing normal bath solution (data not shown), but impedes the accurate estimation of charge transfer of hypertonic sucrose-evoked mEPSCs. We eliminated this artifact and obtained the more precise estimation of the charge transfer by separating the baseline from the recorded trace and thus isolating the mEPSC signals. The data procession is as shown:

a. Original trace

b. Creating a preliminary baseline trace (blue) as the upward outline of the recorded trace, which was obtained by applying a low pass filter and then a maximum value filter (with a mask size=4.5 ms, the value of the data point is selected to be the maximal value in the time range of ±2.25 ms) over the recorded trace

c. Gapping the disrupted baseline trace during the burst of mEPSC firing

d. Estimating the baseline during the gap as a polynomial fitting.

e. Comparing the value of preliminary baseline and polynomial fitting, selecting the max value to be the value of the data point and thus to obtain the estimated baseline trace

f. The baseline (blue) can be separated from the recorded trace (red)

g. Making the subtraction of the baseline trace from the recorded trace(**a**) to get the estimated sucrose triggered mEPSC which was ready for calculating the charge transfer.

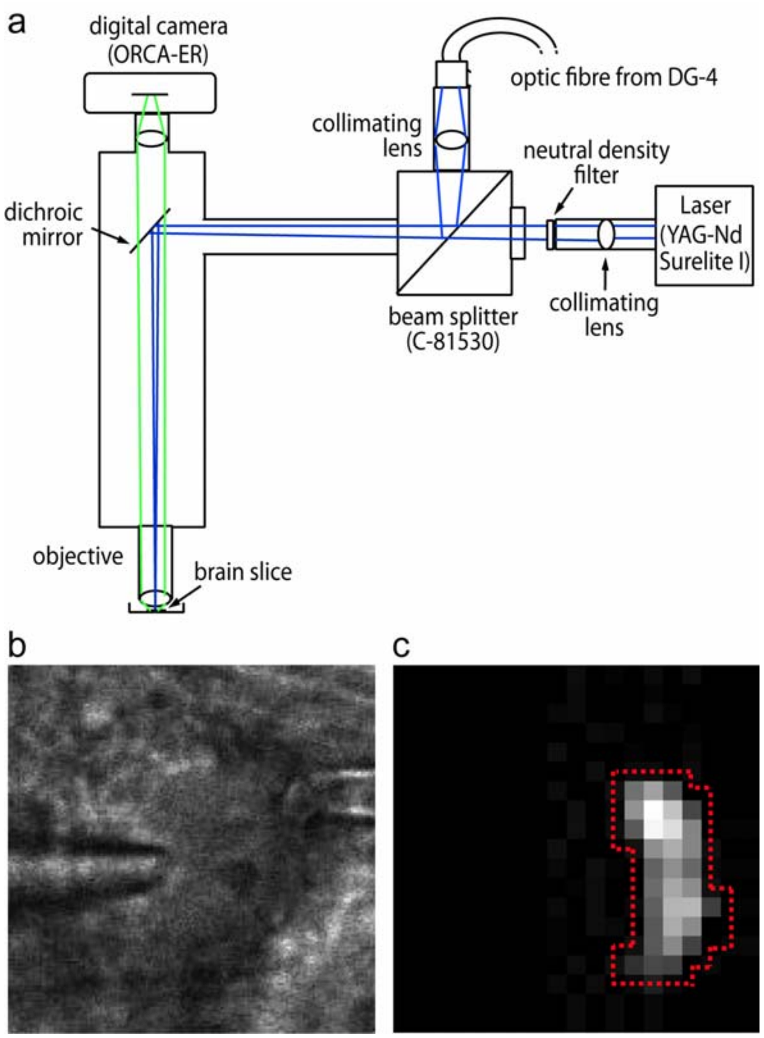

Supplementary Figure 10

Ca^{2+} uncaging and Ca^{2+} imaging.

a. Schematic view of the electrophysiology setup used for experiments involving simultaneous Ca^{2+}-uncaging, Ca^{2+}-indicator dye monitoring of the $[Ca^{2+}]_i$, and EPSCs. UV pulses from a frequency-tripled YAG-ND laser (Surelite I, Continuum) were conducted into the epifuorescence port of an Axioskop and merged with polychromic light of a monochromator (DG-4, Sutter Instrument) using a beam-splitter (customized 90%T10%R for 355 nm with a bandwidth of <10nm [Chroma]). Both UV light beams were collimated to optimize their intensity on the targeted terminal. A CCD camera (ORCAR-ER, Hamamatzu) with on-chip binning (19×19 pixels) was used to capture fluorescence images of the terminals when the Ca^{2+}-indicator dyes were excited at 340 and 380 nm. **b** and **c**. Representative IR-DIC (b) and fluorescence image (c; dotted red line = area used for ratiometric measurements of $[Ca^{2+}]_i$). Image capture and analysis was performed using MetaFluor software, with fura-2, fura-4F and fura-6F, as Ca^{2+} indicator dyes (pentapotassium salts, Molecular Probes, Oregon, USA) to monitor $[Ca^{2+}]_i$ over the following ranges, respectively: 0-250 nM, 0.25-3.4 μM and 3.4-14.0 μM.

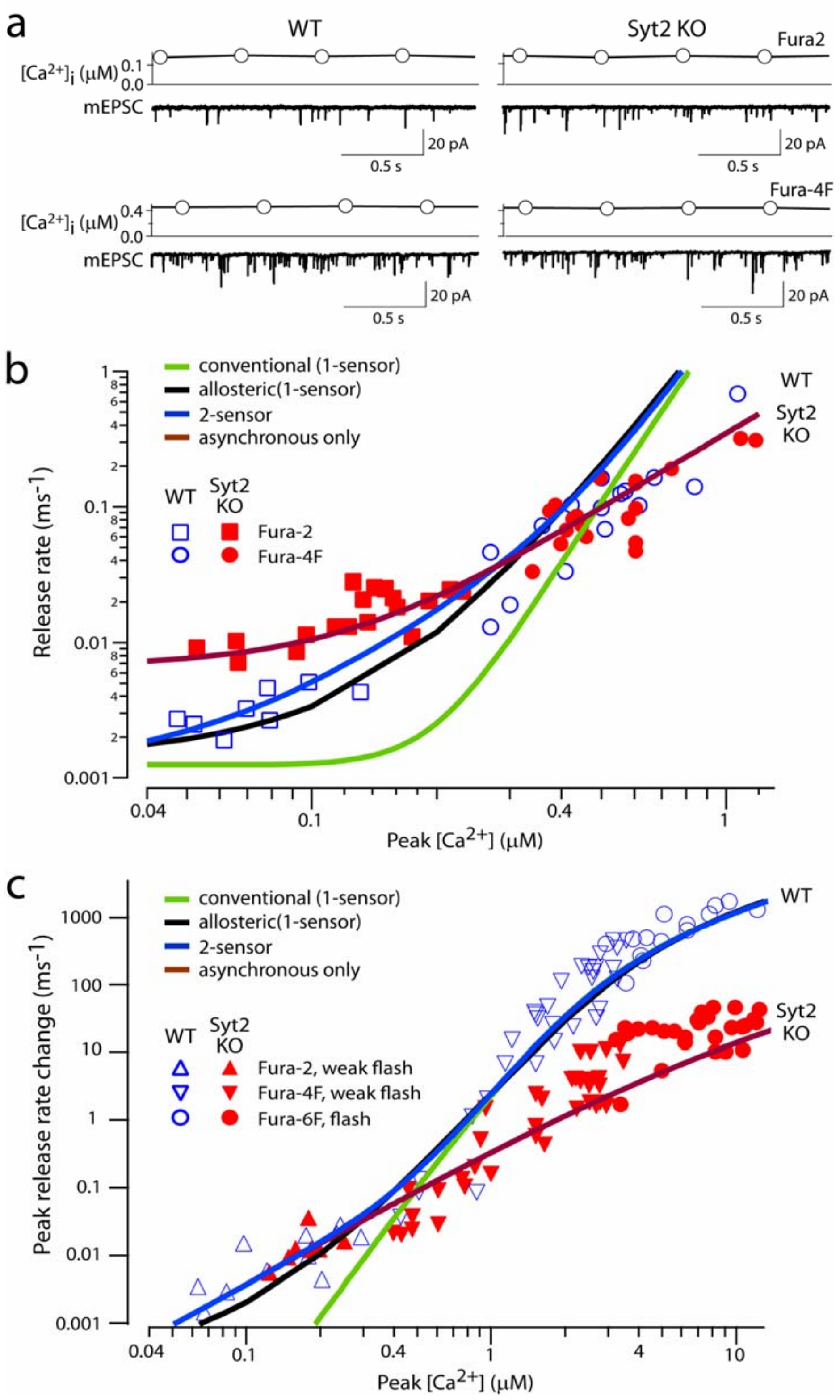

<u>**Supplementary Figure 11**</u>

Vesicular release rates at various $[Ca^{2+}]_i$ in calyx terminals.

The figure compares the release rates obtained after intracellular dialysis of Ca^{2+} clamped with a buffer (a,b) to that obtained with flash photolysis of Ca^{2+} (c). The data shown in b and c are the same as shown in Fig. 4 of the paper, but separated into the two modes of introducing Ca^{2+} into the terminals in order to allow a comparison of the results.

a. Sample traces from representative experiments recorded in wild-type (left panels) and synaptotagmin-2 deficient calyces (right panels) at two characteristic Ca^{2+}-concentrations; the Ca^{2+}-indicator dyes used are shown on the right. The intracellular $[Ca^{2+}]_i$ were achieved by dialysis of Ca^{2+}-buffers into the terminals via the patch pipette.
b. Summary graph of EPSC release rates and $[Ca^{2+}]_i$ (wild-type [open symbols], synaptotagmin-2 deficient terminals [filled symbols]) measured in response to dialysis of Ca^{2+} buffered to defined concentrations into Calyx terminals via the patch pipette. EPSCs were recorded in the double-patch configuration at P7~P9 in the presence of 0.1 μM tetrodotoxin, 0.1 mM cyclothiazide, 1 mM kynurenic acid, and 50 μM D-AP5; presynaptic $[Ca^{2+}]_i$ was simultaneously monitored optically using different Ca^{2+}-sensitive dyes as indicated. Note that due to the higher mini-frequency rate in the synaptotagmin-2 KO neurons, the release rate is significantly higher in the KO synapses than in wild-type synapses at <160 nM $[Ca^{2+}]_i$. At 160-1,000 nM $[Ca^{2+}]_i$, in contrast, the release rate is identical between wild-type and synaptotagmin-2 KO synapses even without subtraction of the resting mini frequency, and at higher $[Ca^{2+}]_i$, the release rate is lower in the KO synapses.
c. Summary graph of the peak release rates (integrated over 2 sec) and $[Ca^{2+}]_i$ measured in response to flash photolysis of Ca^{2+} (n=56 for wild-type [open symbols], 69 for synaptotagmin-2 KO terminals [filled symbols]; note that the Ca^{2+} dialysis data (panel b) were excluded). The background spontaneous release rate was subtracted from the data shown (but not from the data in Fig. 4 or in panel b above) to correct for the 'unclamping' of spontaneous release induced by the deletion of synaptotagmin-2; this unclamping is Ca^{2+}-independent since it persists at 0 Ca^{2+} (Suppl. Fig. 6 and Suppl. Table 1). Our two Ca^{2+}-sensor model accounts for this clamping by the clamp factor C that modulates the spontaneous release rate γ1 (Fig. 5). The difference in spontaneous release between wild-type and synaptotagmin-2 KO terminals obscures Ca^{2+}-dependent release resulting from the competition between synchronous release and asynchronous release mechanisms especially at low $[Ca^{2+}]_i$. To isolate the release evoked by Ca^{2+} uncaging from the background of spontaneous release, we subtracted spontaneous release rate from the measured release rate after flash photolysis. In **b** and **c**, the solid lines represent the predicted behavior based on the various models for release (green = conventional 1-sensor model[11,12]; black = allosteric 1-sensor model[19]; blue = 2-sensor model for wild-type calyces; brown = 2-sensor model for calyces lacking the fast Ca^{2+}-sensor). In all of the models, the RRP is set to 3000 vesicles[11,12]. In **c**, the data were fitted by these three models in the absence of the spontaneous release term (γ1=0).

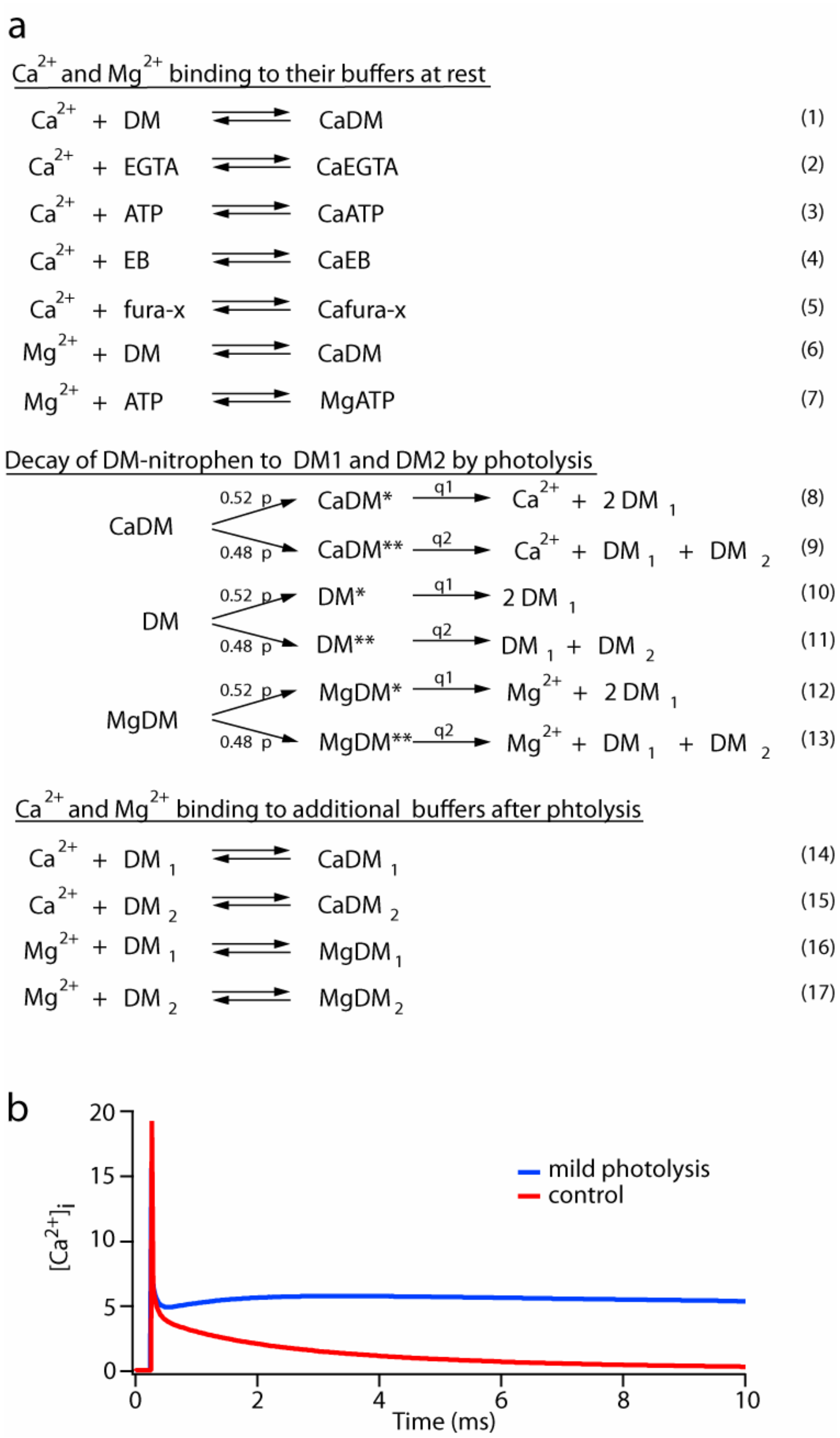

Supplementary Figure 12

Ca^{2+}-relaxation.

We used a Ca^{2+} relaxation model with the parameters from refs. 6-9 to estimate the $[Ca^{2+}]_i$ time course.

a. The reactions (1)-(7) describe the kinetics of Ca^{2+} and Mg^{2+} buffering before photolysis, which reach to an equivalent status with free $[Ca^{2+}]_i$ <100 nM (measured both in vivo and in vitro). The reactions (8)-(17) describe the photolyzing process of CaDM-nitrophen, MgDM-nitrophen and

nitrophen during and shortly after photolysis. *p* is the rate of photolysis, with which a fraction of caged compounds decomposed into two subphotoproducts, CaDM*, CaDM**, DM*, DM**, MgDM*, MgDM**, with different percentages (52% and 48%). q_1 and q_2 are the rate of uncaging, with which two types of subproducts start to uncage Ca^{2+}, Mg^{2+} and other photoproducts DM_1 and DM_2 after photolysis. Reactions (14)-(17) describe the kinetics that new produced DM_{-1} and DM_{-2} further interact with Ca^{2+} and Mg^{2+} as buffers. The reactions (1)-(7) along with (14)-(17) describe the kinetics of Ca^{2+} and Mg^{2+} buffering after photolysis.
b. Example of the $[Ca^{2+}]_i$ decay time course when the laser pulse uncaged 7% of CaDM and followed by a mild photolysis produced by UV from monochromator (presumably 0.000044% corresponding to a ~20 Hz imaging capturing frequency, 340/380 UV exposure time=0.6 s every second). It is predicted that mild photolysis with only 10^{-5} of the laser power is sufficient to keep the $[Ca^{2+}]_i$ elevated for a long time.

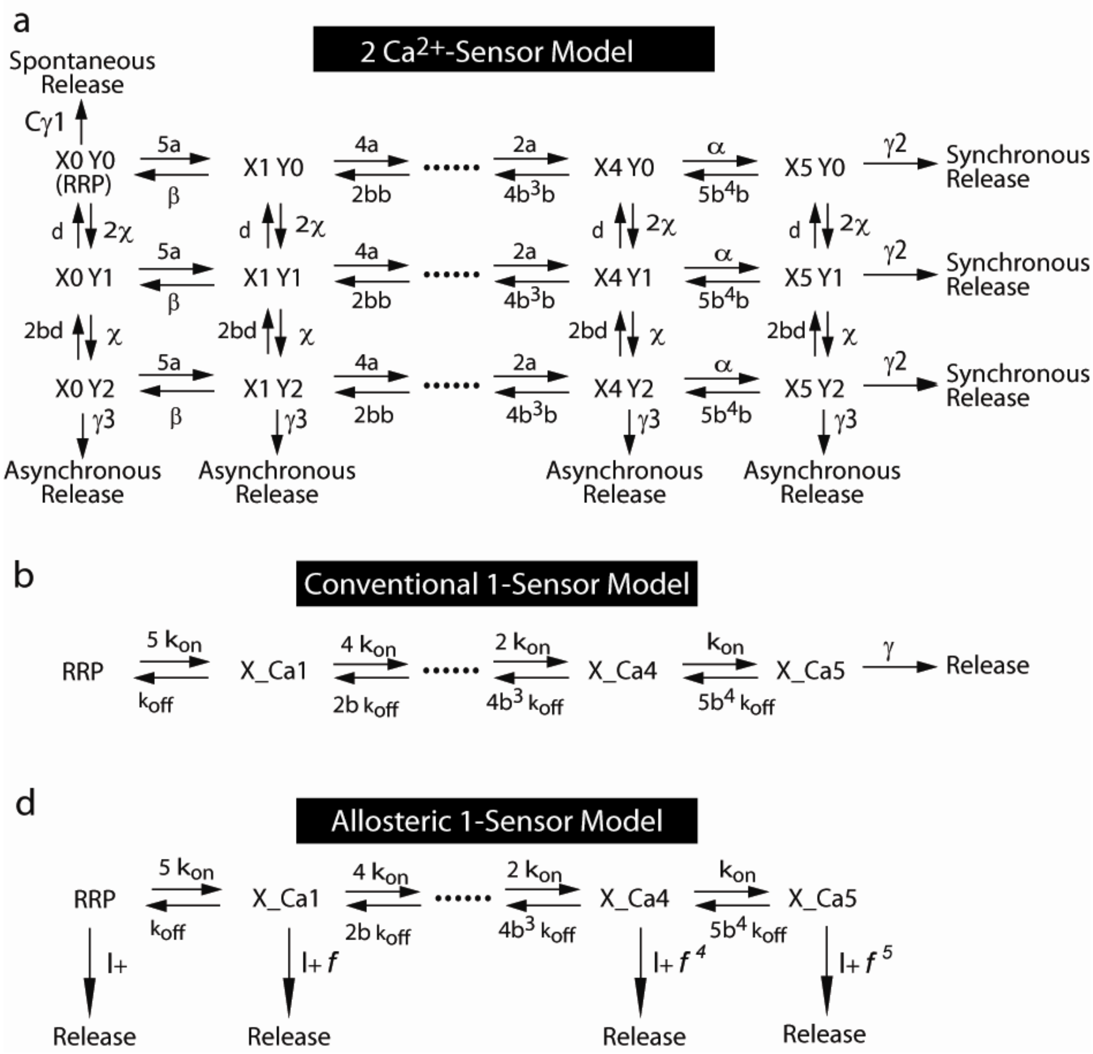

Supplementary Figure 13

Quantitative models of release used for data fitting

a. Two Ca^{2+}-sensor model (see legend to Fig. 5).

b. Conventional one Ca^{2+}-sensor model[8,13]. Parameters: k_{on}=1.53*10^{8} M^{-1}s^{-1}, k_{off}=5800 s^{-1}, γ=6000 s^{-1}, b=0.25 (adjusted from [13]; Bollman et al. proposed a mechanistically similar model[8]).

c. Allosteric one Ca^{2+}-sensor model[7]. Parameters: k_{on}=1.80*10^{8} M^{-1}s^{-1}, k_{off}=3000 s^{-1}, l_{+}= 4.17*10^{-4} s^{-1}, f=27.0, b=0.5. In all models, the RRP size is set to 3000 vesicles.

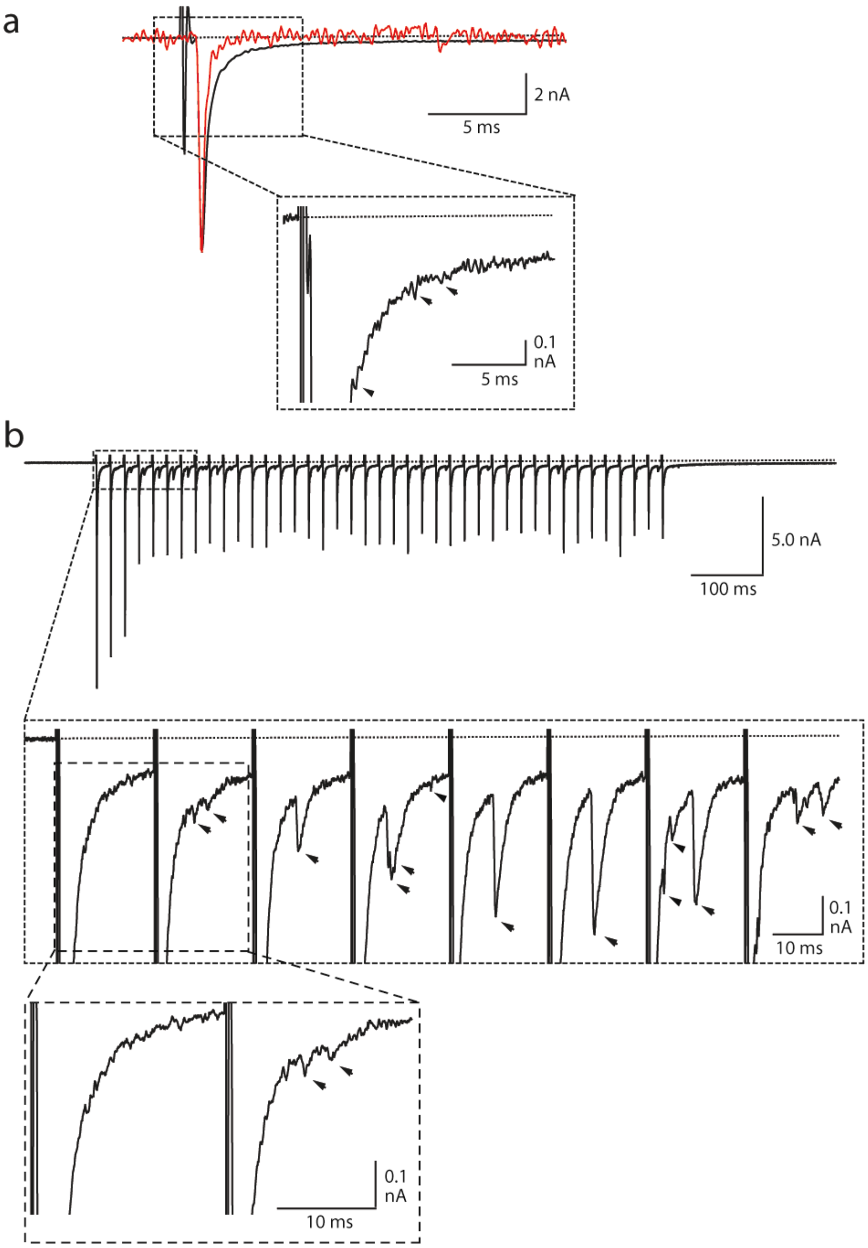

Supplementary Figure 14

Asynchronous component during a single action potential evoked EPSCs.

In rats, a prominent asynchronous release component has been found in EPSCs evoked by isolated APs at physiological temperature[16]. Moreover, the appearance of a massive stimulation-dependent increase in mini frequency during an AP train has suggested the existence of asynchronous release in intact Calyx synapses[18]. In our experiments, postsynaptic voltage-clamp recordings of EPSCs were evoked in the presence 50 µM D-AP5 by afferent fiber stimulation in P14 wild-type calyx synapses at 34 °C. mEPSCs were also obtained from the same traces, and averaged (n=11) by aligning them with their onsets.

a. A representative EPSC evoked by an isolated AP (black) was superimposed with the scaled average mEPSCs (red; n=11, from the same trace with inter-mEPSC intervals of >20 ms). The expansion displays the evoked EPSC on a larger scale; arrows indicate quantal-like events. Note

that the decay time course exhibits a significance difference between EPSC and mEPSCs recorded from the same cells as noted previously[16]. The slow component of the EPSC lasts longer than 20 ms, whereas mEPSCs usually decay back to baseline within 5 ms. A detailed observation of the late phase of EPSCs reveals that quantal-like events can often be observed in EPSCs recorded at 34 °C from P14 mice as indicated by the arrows in the expansion (observed in >70% of cells (n=53)).
c. EPSCs in response to a 50 Hz AP trains induced by fiber stimulation at 34 ºC. Expansions of parts of the EPSCs are shown below. The quantal-like events are increased during the stimulus train, and often consist of multiple simultaneous quanta (arrowheads). The events are not an artifact or due to AMPA channel noise[17] because they always occur during a late phase of high frequency stimulation (100%, n=53) in which these quantal-like events are well shaped as asynchronous EPSCs (b). The results demonstrate that asynchronous release is an intrinsic component of transmitter release in mature calyx of Held.